OPTICA

Quantum super-resolution microscopy by photon statistics and structured light

F. Picariello,[1,2,*] E. Losero,[2] S. Ditalia Tchernij,[3,4] P. Boucher,[5] M. Genovese,[2,3] I. Ruo-Berchera,[2] and I. P. Degiovanni[2,3]

[1]Department of Electronics and Telecommunications, Politecnico di Torino, Turin, Italy
[2]Istituto Nazionale di Ricerca Metrologica, Turin, Italy
[3]Physics Department, University of Torino, Turin, Italy
[4]Istituto Nazionale di Fisica Nucleare sez., Torino, Italy
[5]Quantonation, Paris, France
*fabio.picariello@polito.it

Received 28 August 2024; revised 19 January 2025; accepted 4 March 2025; published 2 April 2025

Reaching high-resolution imaging of delicate samples at a low-intensity level is a major challenge in microscopy. Here, we present and experimentally implement an advanced quantum super-resolution imaging technique based on photon statistics measurement. Our reconstruction algorithm adapts to any kind of non-Poissonian emitters, outperforming the corresponding classical SOFI method, in particular in low-light conditions. It offers sub-diffraction resolution improvement that scales with the $\sqrt{j}$, where j is the highest-order central moments of the photocounts. More remarkably, we show that in combination with structured illumination, an improvement of $j+\sqrt{j}$ can be reached, providing a promising avenue for non-invasive super-resolution microscopy.

https://doi.org/10.1364/OPTICA.540264

1. INTRODUCTION

Improving spatial resolution is critical in current biological and medical research [1]. Within the principle of optical diffraction, Ernst Abbe initially identified the optical resolution limits as imposed by the numerical aperture of the objective and the wavelength of light [2]. For more than a century, it was considered an impassable limit. However, in the early 1990s, novel approaches broke beyond Abbe's limit by circumventing some of its underlying assumptions (explicit or implicit), among them the linear and static response of the sample to incident light, the far-field intensity detection, and uniform illumination. In particular, by exploiting the non-linear or randomly selective response of point-like fluorescence markers, pioneering techniques such as stimulated emission depletion (STED) microscopy and single-molecule localization microscopy (SMLM) have substantially advanced the field and demonstrated exceptional resolution enhancement [3–6]. However, biologists often demand live cell imaging technologies that provide high resolution while minimizing photodamage when using photosensitive samples, which limits the applicability of the aforementioned techniques in a biocompatible context [7–10].

A biocompatible super-resolution approach that does not require high illumination levels is super-resolution optical fluctuation microscopy (SOFI) [11–14], which exploits the natural or induced random fluctuation of fluorophores' brightness. However, as we will discuss later, SOFI, like some more advanced methods built on it (e.g., [15]), is based on a semi-classical model of light that only contemplates classical super-Poissonian emitters, does not take into account quantum fluctuation, and leads to a strongly limited resolution enhancement in low-light scenarios. In low-light regimes, photon quantization emerges, and a full quantum description is essential for optimal optical imaging [16,17], often exploiting quantum features such as entanglement [18,19] and squeezing [20]. This field, referred to as quantum imaging (see [21] for a recent review), has enabled advancements such as sub-shot-noise imaging and sensing [22–26], quantum-enhanced AFM [27], optical tweezers and non-linear microscopy [28,29], image distillation from noise [30], and imaging/spectroscopy with undetected photons [31–33] to cite a few.

The use of quantum anti-bunching in single-photon emitters to achieve super-resolution via higher-order photo-count correlation functions was first proposed in [34] and later experimentally demonstrated both in wide-field [35] and in confocal settings [36]. Those last methods can be seen as the equivalent of SOFI but for sub-Poissonian emitters.

This paper aims to introduce a full quantum method for super-resolution named quantum super-resolution imaging by photon statistics (QSIPS) that is based on a rigorous full quantum model describing the photon emission and detection. Our model yields a generalized SOFI approach that works optimally at any intensity level and with any non-Poissonian emitter, including single-photon emitters and any kind of blinking (photoswitching) fluorophores. Here, we present the model together with simulations and experimental results, demonstrating the superiority of our approach over traditional SOFI methodologies published in

the literature. The QSIPS super-resolved image is actually the incoherent sum of the power j of each emitter's point spread function (PSF), where j is the highest-order central moments evaluated at each point of the image plane. Thus, assuming a Gaussian PSF, the application of QSIPS provides an enhancement of the resolution of a factor $\sqrt{j}$, corresponding to the effective narrowing of the function $(\mathrm{PSF})^j$.

Furthermore, we present the integration of our QSIPS method with structured illumination microscopy (SIM) [37]. In SIM, the sample is illuminated with a set of non-uniform patterns, and the final super-resolved image is reconstructed by the combination of all the single-pattern images. SIM doubles the maximum frequency information retrieved by the optical system. The integration of non-Poissonian super-resolution methods with SIM has been demonstrated theoretically to provide a much more favorable $j+\sqrt{j}$ super-resolution scaling with the correlation order [38], and the principle has been applied experimentally both for wide-field SOFI [39] and for quantum image scanning microscopy [40]. Here, we demonstrate that even in combination with structured light, our QSIPS method outperforms the classical implementation with SOFI, especially in scenarios characterized by low-light illumination.

2. SUPER-RESOLUTION MODEL

Consider a system of N_c emitters with mutually incoherent and statistically independent emissions. Let $P_\alpha(m)$ denote the probability of emitting m photons from the αth source. Each photon possesses a certain probability of being detected at position $\mathbf{r}$ in the detector plane, denoted as $\eta_\alpha(\mathbf{r})=\rho_\alpha \mathrm{PSF}_\alpha(\mathbf{r})$, where ρ_α accounts for all the optical losses in the setup, including the non-unit efficiency of the detector. Here, $\mathrm{PSF}_\alpha(\mathbf{r})$ represents the imaged system point spread function related to the αth emitter. The effect of the position-dependent loss, $\eta_\alpha(\mathbf{r})$, alters the detected photon distribution at the image plane. In particular, the detected distribution for the αth emitter, denoted as $\mathcal{P}_\alpha(n,\mathbf{r})$, can be expressed according to a binomial statistical model as

$$\mathcal{P}_\alpha(n,\mathbf{r})=\sum_{m=n}^{\infty} P_\alpha(m)\binom{m}{n}[\eta_\alpha(\mathbf{r})]^n[1-\eta_\alpha(\mathbf{r})]^{(m-n)}, \quad (1)$$

while considering the contribution of all the emitters at position $\mathbf{r}$, we have

$$\mathcal{P}(N,\mathbf{r})=\left(\sum_{n_1=0,\dots n_{Nc}}^{\infty}\mathcal{P}_1(n_1,\mathbf{r})\dots\mathcal{P}_{Nc}(n_{Nc},\mathbf{r})\right)\delta_{N,\sum_\alpha n_\alpha}, \quad (2)$$

that is, for each position $\mathbf{r}$, the convolution of all the emitter contributions.

We can identify a statistical quantity known as the cumulant. In particular, the jth cumulant is obtained by performing the jth derivative of the cumulant-generating function $\mathcal{K}(t,\mathbf{r})$ evaluated at $t=0$:

$$\mathcal{K}_\eta(t,\mathbf{r})=\log\left(\sum_{N=0}^{\infty}e^{tN}\mathcal{P}(N,\mathbf{r})\right), \quad (3)$$

$$k_\eta^{(j)}(\mathbf{r})=\frac{d^j\mathcal{K}}{dt^j}(t,\mathbf{r})|_{t=0}, \quad (4)$$

where $k_\eta^{(j)}(\mathbf{r})$ refers to the jth cumulant of the overall detected photon distribution evaluated in the position $\mathbf{r}$ of the detector plane that, for independent emitters, can be written as the sum of each emitter cumulant $k_{\alpha,\eta}^{(j)}(\mathbf{r})$:

$$k_\eta^{(j)}(\mathbf{r})=\sum_{\alpha=1}^{N_c}k_{\alpha,\eta}^{(j)}(\mathbf{r}). \quad (5)$$

The classical SOFI technique relies on assessing the auto-cumulants of the detected photon distribution [11]. Therefore, the jth-order super-resolved signal is evaluated as

$$\mathrm{SOFI}^{(j)}(\mathbf{r}):=k_\eta^{(j)}(\mathbf{r})=\sum_{\alpha=1}^{N_c}k_{\alpha,\eta}^{(j)}(\mathbf{r}). \quad (6)$$

This classical approach, however, does not properly take into account the quantum noise deriving from the discrete nature of the photons. To properly understand what is the origin of the limit of the SOFI technique, we write the second- and third-order super-resolved map evaluated with classical SOFI, explicating the PSF contributions $\eta_\alpha(\mathbf{r})$ to the signal:

$$\mathrm{SOFI}^{(2)}(\mathbf{r})=\sum_{\alpha=1}^{N_c}\left[[\eta_\alpha(\mathbf{r})]^2\left(z_\alpha^{(2)}-z_\alpha^{(1)}\right)+\eta_\alpha(\mathbf{r})z_\alpha^{(1)}\right], \quad (7)$$

$$\mathrm{SOFI}^{(3)}(\mathbf{r})=\sum_{\alpha=1}^{N_c}\left[[\eta_\alpha(\mathbf{r})]^3\left(z_\alpha^{(3)}-3z_\alpha^{(2)}+2z_\alpha^{(1)}\right)+3[\eta_\alpha(\mathbf{r})]^2\left(z_\alpha^{(2)}-z_\alpha^{(1)}\right)-2\eta_\alpha(\mathbf{r})z_\alpha^{(1)}\right], \quad (8)$$

with the terms $z_\alpha^{(j)}$ being the cumulant of a generic order j of the emitted photon distribution $P_\alpha(m)$, evaluated starting from the cumulant-generating function $Z_\alpha(t)$:

$$Z_\alpha(t)=\log\left(\sum_{m=0}^{\infty}e^{tm}P_\alpha(m)\right), \quad (9)$$

$$z_\alpha^{(j)}=\frac{d^jZ_\alpha}{dt^j}(t)|_{t=0}. \quad (10)$$

Note that, in Eq. (7), the only presence of the terms proportional to $[\eta_\alpha(\mathbf{r})]^2$ would correspond to a shrink of a factor $\sqrt{2}$ of each PSF and would lead to a corresponding super-resolved image. However, the other terms, linear with $\eta_\alpha(\mathbf{r})$, are what limit the maximum resolution enhancement. These linear terms originate from the randomness of a loss process when taking into account the discreteness of photons. The same consideration holds for the achievement of third-order super-resolution in Eq. (8), which is limited by the presence of terms in $\eta_\alpha(\mathbf{r})$ and in $[\eta_\alpha(\mathbf{r})]^2$.

For the second-order signal in Eq. (7), we can see that the second-order SOFI fails when the linear terms in $\eta_\alpha(\mathbf{r})$ dominate. Considering that the first-order cumulant is the mean value of the emitted photon distribution, $z_\alpha^{(1)}=\langle m_\alpha\rangle$, and the second-order cumulant is the variance, $z_\alpha^{(2)}=\langle\Delta^2 m_\alpha\rangle$, the condition becomes

$$\eta_\alpha(\mathbf{r})\left(F_\alpha^{(e)}-1\right)\le 1, \quad (11)$$

where we have introduced the Fano factor of the emitted photon distribution relative to the αth emitter as $F_\alpha^{(e)}:=\langle\Delta^2 m_\alpha\rangle/\langle m_\alpha\rangle$. Finally, using the general relation between the Fano factor before

and after an optical loss η, $F^{(d)} = \eta(F^{(e)} - 1) + 1$, we can rearrange Eq. (11) in terms of the Fano factor of the detected photon distribution as

$$F_\alpha^{(d)}(\mathbf{r}) \leq 2. \tag{12}$$

This condition can be used as a rule of thumb to understand when the SOFI technique fails to attain the maximum resolution enhancement due to contributions of lower-order power in the shrinking of the PSF.

The regime dictated by Eqs. (11) and (12) is a characteristic either of high-loss systems [i.e., extremely low values of $\eta_\alpha(\mathbf{r})$] or of sub-Poissonian emitters, i.e., with $0 \leq F^{(e)} < 1$. Particularly, we can see this by considering that an ideal single-photon emitter possesses a probability density function such that all the cumulants are identically null, except the first-order one (i.e., the mean value of the distribution). Subsequently, the second- and third-order SOFI signals become

$$\mathrm{SOFI}^{(2)}(\mathbf{r}) = \sum_{\alpha=1}^{N_c} \eta_\alpha(\mathbf{r}) z_\alpha^{(1)} \left[1 - \eta_\alpha(\mathbf{r})\right], \tag{13}$$

$$\mathrm{SOFI}^{(3)}(\mathbf{r}) = \sum_{\alpha=1}^{N_c} 2\eta_\alpha(\mathbf{r}) z_\alpha^{(1)} \left[[\eta_\alpha(\mathbf{r})]^2 - \frac{3}{2}\eta_\alpha(\mathbf{r}) - 1\right]. \tag{14}$$

Since $\eta_\alpha(\mathbf{r}) < 1$, all SOFI signals evaluated for a system of single-photon emitters do not provide super-resolved maps due to the dominance of the first order of the PSF with respect to higher ones.

Here, we propose a new algorithm for super-resolution, the QSIPS, that overcomes the above-described SOFI limitations, efficiently eliminating the lower-order contributions in the shrinking of the PSF from the super-resolved signal and therefore extending its usage to sub-Poissonian photon sources. In particular, the complete super-resolved signal of order j, $\mathrm{QSIPS}^{(j)}$, can be obtained by performing a linear combination of cumulants of the detected photon distribution as

$$\mathrm{QSIPS}^{(j)}(\mathbf{r}) := \sum_{i=1}^{j} \beta_{i,j} k_\eta^{(i)}(\mathbf{r}) = \sum_{\alpha=1}^{N_c} [\eta_\alpha(\mathbf{r})]^j \left(\sum_{i=1}^{j} \beta_{i,j} z_\alpha^{(i)}\right), \tag{15}$$

where we demonstrate that the coefficients $\beta_{i,j}$ coincide with the Stirling number of the first type [41]:

$$\beta_{i,j} = \frac{1}{i!}\frac{d^i}{dx^i}\prod_{k=0}^{j-1}(x-k)|_{x=0} = S_I(i,j). \tag{16}$$

Equation (15) shows how to properly combine cumulants up to the jth order to derive a signal proportional uniquely to $[\eta_\alpha(\mathbf{r})]^j$. This super-resolution method applies to all kinds of non-Poissonian photon sources, and it is completely independent of the optical losses, therefore ensuring the maximum super-resolution enhancement in all levels of illumination.

Another way to rewrite Eq. (15) more compactly is to exploit the factorial cumulant-generating function:

$$\mathcal{S}_\eta(\rho, \mathbf{r}) = \log\left(\sum_{N=0}^{\infty} \rho^N \mathcal{P}(N, \mathbf{r})\right). \tag{17}$$

The peculiarity of this generating function is that its moment of order j, evaluated performing the jth derivative of Eq. (17) at $\rho = 1$, retrieves the exact linear combination of cumulants of the detected photon distribution from order 1 to j, reported in Eq. (15), with coefficients $\beta_{i,j}$. Therefore, the super-resolved relation of order j reported in Eq. (15) can be rewritten as

$$\mathrm{QSIPS}^{(j)}(\mathbf{r}) = \frac{d^j \mathcal{S}_\eta}{d\rho^j}(\rho, \mathbf{r})|_{\rho=1}. \tag{18}$$

The proof of Eqs. (15)–(18), with the requirement of non-Poissonianity of the sources, is reported in Supplement 1.

In our experiment, we exploited, as a specific example of non-Poissonian photon sources, quantum dot (QD) nanoparticles that exhibit blinking behavior. Even though QDs can be treated as single-photon emitters, the presence of trap states can lead the photon source to a temporary "off" state, which emits non-radiatively [42]. This blinking characteristic is what gives rise to super-Poissonian photon statistics. To ensure proper interpretation of the experimental results, we carry out simulations where we have considered QDs with super-Poissonian behavior as the ones in our experiment and with sub-Poissonian statistics as ideal single-photon emitters. We considered the QDs as uncorrelated independent emitters that undergo M_α excitation cycles in a single exposure time. The blinking nature of the emitters is considered by associating with each excitation cycle a certain probability b_α, noted as blinking probability, in which no photon is emitted. The probability density function related to the emission of a generic emitter α is modeled as

$$P_\alpha(m) = b_\alpha \delta_{m,0} + (1 - b_\alpha)\delta_{m,M_\alpha}. \tag{19}$$

The emitted photon's Fano factor can be evaluated as $F_\alpha^{(e)} = M_\alpha b_\alpha$, with the condition $M_\alpha b_\alpha > 1$ ensuring super-Poissonian statistics, while the condition reported in Eq. (11) becomes

$$\eta_\alpha(\mathbf{r})\,(M_\alpha b_\alpha - 1) \leq 1. \tag{20}$$

3. METHODS

The experimental setup employed in this study is a conventional wide-field fluorescence optical setup with the addition of a spatial light modulator (SLM) for structured illumination. A schematic representation of the experimental setup employed is depicted in Fig. 1.

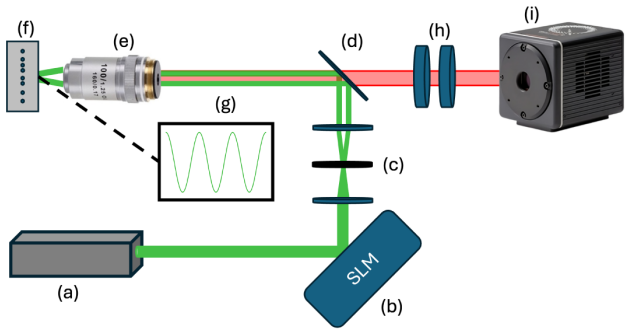

Fig. 1. Experimental setup schematic: (a) 532 nm CW laser; (b) spatial light modulator; (c) Fourier optics and rotating mask; (d) dichroic mirror (550 nm cutoff); (e) 100× air objective; (f) CdSe/ZnS QDs (emission at 620 nm); (g) interference pattern at the focal plane; (h) 600 nm long-pass and 700 nm short-pass filters; and (i) CMOS camera.

The system consists of a 532 nm CW laser interacting with the SLM, which imposes a spatially changing phase shift on the incoming light wavefront. The interference pattern is constructed by imposing a 2D cosinusoidal pattern on the SLM, as shown in Eq. (21), using a MATLAB script with fixed values of θ and ϕ. In this way, the SLM acts as a diffraction grating, producing in the far field (obtained by a lens) an interference pattern. We select the first two maxima of the interference through a rotating mask, which passes through a second focus-adjusting lens and dichroic mirror with a 550 nm cutoff. The beam is then focused using a 100× air objective onto a glass substrate containing commercial colloidal CdSe/ZnS QDs, which exhibit a fluorescence emission peak at 620 nm with an FWHM of 20 nm. To create the QD samples, a toluene solution containing QDs was put on a glass slide and then diluted with an isopropyl alcohol solution to reduce the QD concentrations. To ensure a uniform distribution of emitters, the sample was spin-coated for 60 s at 100 rps. The fluorescence is then transmitted via the dichroic mirror, filtered by a 600 nm long-pass and a 700 nm short-pass filter, and captured by a CMOS camera. The Hamamatsu ORCA-QUEST C15550-20UP CMOS camera was utilized in this experiment, characterized by a low readout noise RMS of $0.23e^-$ and a high quantum efficiency of 85% at 460 nm and ∼70% at 620 nm.

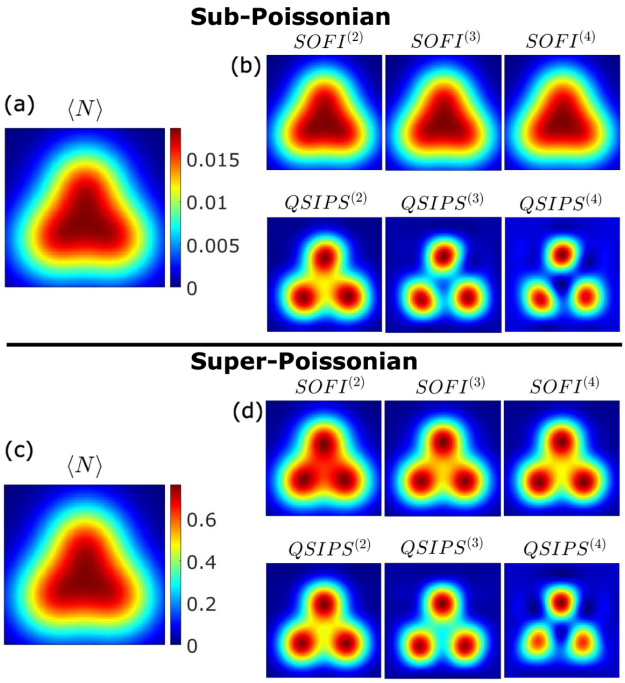

Fig. 2. Simulation of three identical non-Poissonian emitters in a noiseless scenario with standard deviation of the PSF (σ) of 1.2 and spaced $1.15 \times \sigma$ in pixel units. (a) The mean number of detected photons from ideal non-blinking single-photon emitters ($b_\alpha = 0$ and $M_\alpha = 1$ for any α). (b) SOFI and QSIPS super-resolved images up to the order 4 for single-photon emitters evaluated by 3×10^6 independent frames. (c) Mean number of detected photons for blinking super-Poissonian emitters ($b_\alpha = 0.7$ and $M_\alpha = 70$ for any α). (d) SOFI and QSIPS super-resolved images up to the order 4 for blinking emitters evaluated by 1×10^5 independent frames. All simulations are performed by setting an optical loss $1 - \rho_\alpha = 0.75$, which does not include the further effect of PSF's spatial spreading. Fourier interpolation and Gaussian filtering have been applied to improve image quality and reduce noise.

4. RESULTS AND DISCUSSION

A simulation was conducted in MATLAB on three closely spaced, identical emitters, each with the probability density function $P_\alpha(m)$ reported in Eq. (19). The detection scheme consists of a matrix of ideal, noise-free photon-number-resolving detectors in an optical system with unitary magnification, each pixel characterized by a probability of detecting N photons $\mathcal{P}(N, \mathbf{r})$ according to Eq. (2). Individual detector images were temporally averaged to generate a classical intensity map $\langle N \rangle$, while the super-resolution images were obtained by assessing the auto-cumulant operation separately to each pixel using both QSIPS and SOFI techniques.

Figure 2 shows two distinct cases: the top panel presents both super-resolution methods, up to the fourth order, employing ideal non-blinking single-photon emitters (i.e., sub-Poissonian photon sources), while the bottom panel refers to the presence of a blinking characteristic that gives rise to the super-Poissonian behavior. Particularly, we can notice that in the sub-Poissonian case, the SOFI method fails to provide any resolution enhancement, as suggested by Eqs. (13) and (14), while in the super-Poissonian one, the increase in resolution is only partially achieved. Nevertheless, our QSIPS method demonstrates its ability to enhance the spatial resolution regardless of the photon statistics considered.

In Fig. 3, we report the simulation study of the super-resolution visibility in the case of super-Poissonian emitters. The visibility is accessed in terms of the relative deepness of the valley between two identical blinking emitters obtained in the second-order super-resolved images via SOFI and QSIPS methods [see the examples reported in Figs. 3(a) and 3(b)]. Figure 3(c) shows that the QSIPS maintains constant visibility at all levels of illumination and for all values of the detected Fano factor. In contrast, the visibility gained with the traditional SOFI method grows with the number of detected photons and the corresponding Fano factor, according to the discussion of Eq. (12), finally reaching the QSIPS's performance for $F^{(d)} \gg 1$.

An experimental demonstration of the superiority of QSIPS with respect to SOFI has been performed employing the setup described in Section 3, without adding structured illumination by imposing a uniform pattern on the SLM. In particular, Figs. 4(a)–4(d) display the intensity map along with the super-resolved images of a small cluster of QDs and a 1D plot to showcase the resolution enhancement. In particular, the fourth-order QSIPS reconstruction shows the inner structure of the cluster that cannot be unveiled by the standard SOFI. To quantify the real super-resolution improvement, we investigated the narrowing of the effective (super-resolved) PSF for an isolated emitter in function of the super-resolution order j. The analysis is based on a 2D Gaussian fit of the effective PSFs applied to each super-resolution order. A normalization of the size of each super-resolved PSF with the one of the intensity's PSF is applied. The result is illustrated in Figs. 4(e) and 4(f), which refer to two different exposure times. The experimental data for SOFI (orange stars) and QSIPS (blue dots) are compared with the theoretical expected scaling of $1/\sqrt{j}$ (yellow curve). We can see that in the high illumination regime of Fig. 4(f), both approaches coincide with the theoretical prediction; however, with a limited number of detected photons as in Fig. 4(e), the actual resolution boost offered by SOFI is inconsistent across multiple super-resolution orders.

Although this study does not provide experimental results utilizing sub-Poissonian light sources, a version of the QSIPS method, applicable exclusively to single-photon emitters, has been proposed

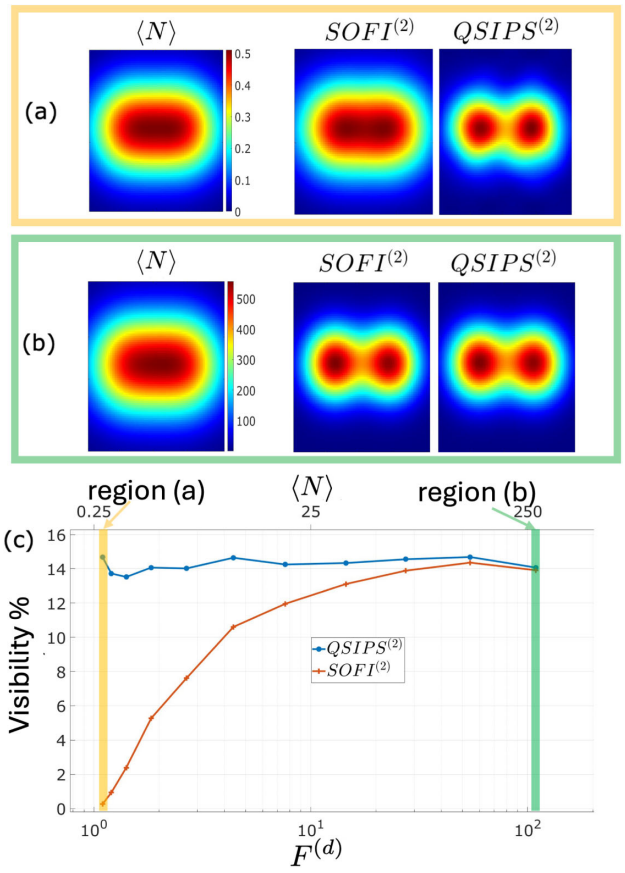

Fig. 3. Visibility comparison of two identical blinking single-photon emitters (simulated) with standard deviation of the PSF (σ) of 1.55 and spaced $1 \times \sigma$ in pixel units. (a) From left to right: mean intensity map, second-order SOFI, and second-order QSIPS maps in the low-photon-number regime, obtained by setting $M_\alpha = 60$ and $b_\alpha = 0.3$ for both emitters. (b) Shows the same quantities, albeit in a strong light regime, with $M_\alpha = 60 \times 10^3$ and $b_\alpha = 0.3$. (c) Visibility of the dip between the emitters in function of the Fano factor (bottom axis) and the mean number of detected photons (top axis) obtained by changing the number of excitations per simulated frame from $M_\alpha = 60$ to $M_\alpha = 60 \times 10^3$. Both the bottom and the top axes refer to the average values of the respective quantities evaluated in the region covered by the PSF of the emitters. The parameters chosen in the examples of (a) and (b) correspond to highlighted yellow and green bars in (c), respectively. All simulations are performed by setting an optical loss $1 - \rho_\alpha = 0.85$, which does not include the further effect of PSF's spatial spreading and a statistical sample of 10^5 frames. The images displayed were Fourier-interpolated to reduce pixelation effects.

and experimentally demonstrated [36]. Supplement 1 illustrates that the mathematical model reported in [36] is a specific instance of our generalized QSIPS method.

A. Integration with Structured Light

The fundamental concept behind SIM is to employ an illumination pattern such as

$$I_{\theta,\phi}(\mathbf{r}) = \frac{I_0}{2}\left[1 - \cos(2\pi\left(\mathbf{p}_\theta \cdot \mathbf{r}\right) + \phi)\right], \tag{21}$$

with $\mathbf{r}$ denoting the spatial position on the object plane and $\mathbf{p}_\theta$ referring to the illumination frequency vector. Combining different acquisitions performed with different values of θ and ϕ by shifting the Fourier components of $\pm|\mathbf{p}_\theta|$ allows covering twice the Fourier space normally achievable with standard illumination, therefore doubling the resolution enhancement [43].

In this work, we focus on integrating second-order super-resolved maps evaluated through non-Poissonian photon statistics with structured light.

The greatest resolution improvement is obtained when the magnitude of $|\mathbf{p}_\theta|$ equals the maximum spatial frequency that the system can broadcast, k_{Abbe}. This frequency is related to the width, σ, of the system's optical PSF as $k_{\text{Abbe}} = 0.42/\sigma$ [44]. The next simulations will use $|\mathbf{p}_\theta| = k_{\text{Abbe}}$. In the following, we present the results of simulations carried on in conditions analogous to the one of Fig. 2, but for the sake of completeness, we also added the contribution of the readout noise to each detection pixel modeled as a Gaussian distribution convoluted with the detected photon statistics. The readout noise represents the main noise contribution in low-light-level situations when employing classical wide-field linear sensors [45]. To add the influence of structured illumination, the emission probability of k photons by each αth emitter becomes

$$\pi_{\alpha,\theta,\phi}(k) = \sum_{m=0}^{\infty} P_\alpha(m)\, B\left(k|m,\, I_{\theta,\phi}(x_\alpha, y_\alpha)\right), \tag{22}$$

where $I_{\theta,\phi}(x, y)$ derives from Eq. (21) by setting $I_0 = 1$, $\mathbf{p}_\theta = |\mathbf{p}_\theta|(\cos(\theta), \sin(\theta))$ and $\mathbf{r} = (x, y)$. Thus, structured light operates as a binomial filter with a transmittance probability of $I_{\theta,\phi}(x_\alpha, y_\alpha)$. The probability of observing n photons at position $\mathbf{r}$ is analogous to Eq. (1), where the probability $\pi_{\alpha,\theta,\phi}(k)$ plays the role of $P_\alpha(m)$. In particular, $\pi_{\alpha,\theta,\phi}(k)$ undergoes a binomial process driven by the combination of PSF and optical losses $\eta_\alpha(x, y)$. Using the detected photon distributions obtained in this way, a series of 20 simulated datasets is created, considering four values of θ and five values of ϕ. For each value of θ and ϕ, second-order super-resolved images are generated using both QSIPS and SOFI methods. Each non-Poissonian super-resolved map encompasses spatial frequency information within a radius of $\sqrt{2}k_{\text{Abbe}}$. By accurately shifting each frequency component in the Fourier space, it is possible to extend the coverage in the reciprocal space up to a factor $2 + \sqrt{2}$ with respect to the region achievable with conventional illumination [38]. The values of θ and ϕ employed in these simulations, as well as in the experimental realization, were $\theta = \{0, \frac{\pi}{4}, \frac{\pi}{2}, \frac{3\pi}{4}\} + \frac{\pi}{8}$ and $\phi = \{0, \frac{2\pi}{5}, \frac{4\pi}{5}, \frac{6\pi}{5}, \frac{8\pi}{5}\} + \frac{\pi}{8}$. First, for each of the 20 combinations of θ and ϕ, the mean intensity map and the second-order super-resolved SOFI and QSIPS maps are evaluated. The corresponding averages of the 20 maps are reported in Figs. 5(a)–5(c). Then the images at the various orientations and phases are Fourier-transformed, Wiener-filtered, and shifted in the Fourier space according to the SIM algorithm [43], using the assessed frequency vector $\mathbf{p}_\theta$. Finally, the frequency components are summed and inverse-Fourier-transformed. The final super-resolved images, labeled as SOFI$^{(2)}$ − SIM and QSIPS$^{(2)}$ − SIM, are shown in Figs. 5(d) and 5(e). The 1D plot along the black-dashed line in Fig. 5(e) is reported in Fig. 5(f). The simulation clearly shows a resolution enhancement of the QSIPS with respect to SOFI maintained when combined with structured illumination.

The setup described in Section 3 was used to experimentally integrate SIM with the QSIPS approach in low-light scenarios. Preliminarily, a high-density sample of colloidal QDs was used to assess the illumination frequency vectors $\mathbf{p}_\theta$ for all orientations. Following that, the same sample used for the analysis in Fig. 4

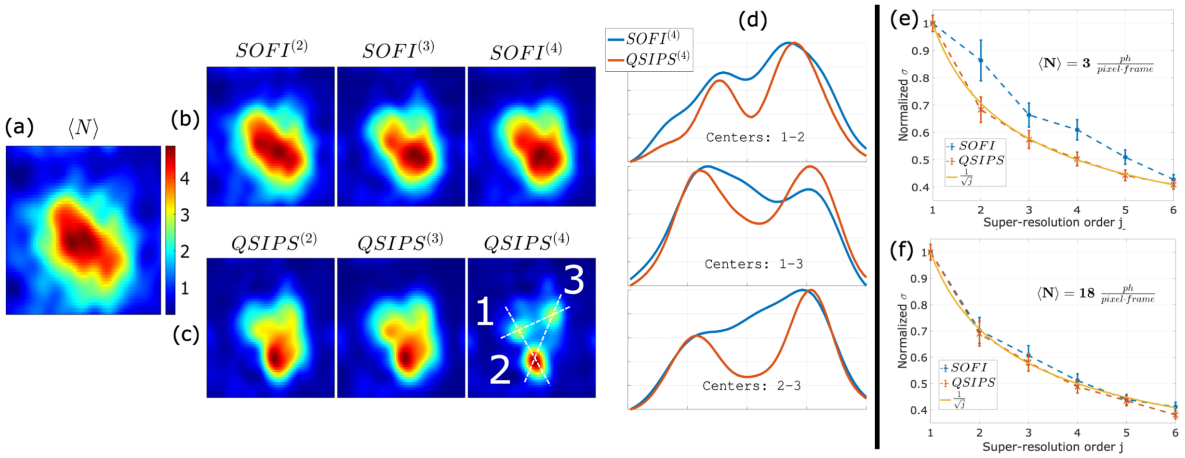

Fig. 4. Experimental comparison between SOFI and QSIPS methods. (a) Mean intensity map of a QDs cluster. (b), (c) First four super-resolution orders' maps obtained using the SOFI and QSIPS approaches, respectively. (d) Normalized fourth-order super-resolution signals in a 1D plot along intersecting axes from the three centers indicated in (c). An exposure duration of 20 ms and a laser power of 1.4 mW were used to capture 53×10^3 frames. Fourier interpolation and Gaussian filtering were used to improve image quality and minimize noise. (e), (f) The y axis shows the (normalized) standard deviation of the effective PSF evaluated for an isolated emitter depending on super-resolution orders (x axis) under two light conditions: $\langle N \rangle = 3$ ph/pixel/frame at 50 ms exposure, and $\langle N \rangle = 18$ ph/pixel/frame at 200 ms exposure, respectively. The SOFI (blue-dashed line) and QSIPS (orange-dashed line) data are represented. The theoretical behavior is shown as a continuous yellow line.

was employed, but focusing on a different cluster whose intensity image is shown in Fig. 5(g). As for the simulation scenario, the SOFI$^{(2)}$ and QSIPS$^{(2)}$ are evaluated for each of the 20 structured illumination patterns, and their average is reported in Figs. 5(h) and 5(i). Afterward, they are combined in Fourier space and transformed back into the real space leading to the super-resolved images in Figs. 5(j) and 5(k). These results also demonstrate experimentally the advantage of QSIPS–SIM in comparison with SOFI–SIM.

To assess the actual super-resolution provided by the integration with structured light, we focused on an isolated emitter and performed a two-dimensional Gaussian fit of the effective PSFs across multiple super-resolution techniques. Particularly, we evaluated the super-resolution enhancement by performing the ratio between the PSF's standard deviation of the intensity image and the one obtained for all the different super-resolution methods. Figure 6 shows the 1D Gaussian fits for both simulation [Fig. 6(a)] and experimental realization [Fig. 6(b)]. The super-resolution enhancement for both simulated and experimental results, as their

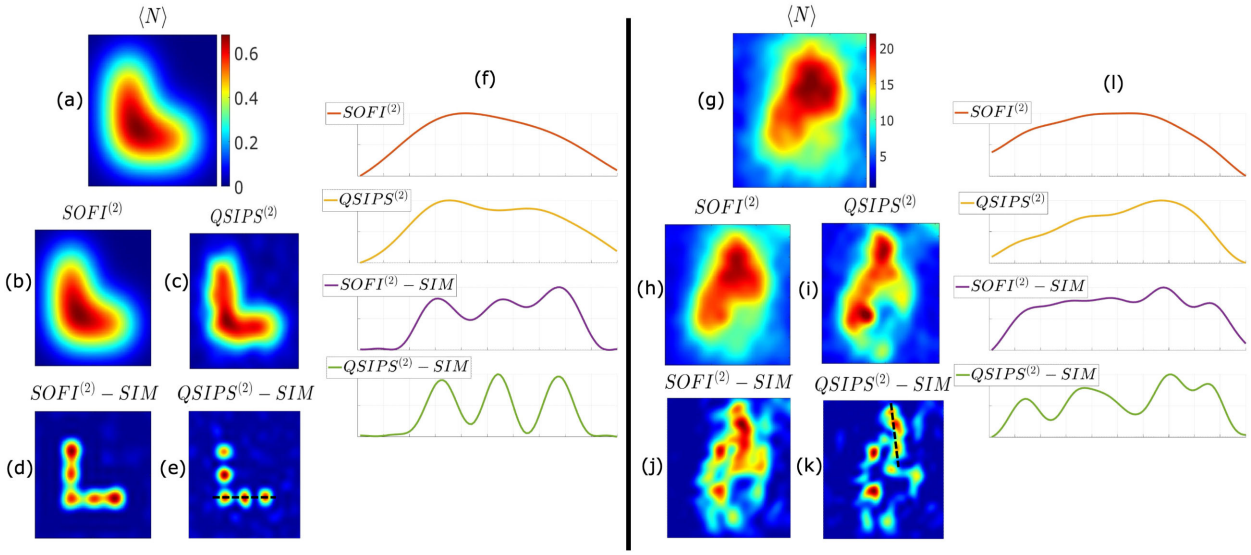

Fig. 5. Second-order SOFI and QSIPS algorithms integrated with SIM. (a)–(f) Simulation results for an L-shaped configuration of identical blinking single-photon emitters using a noisy detection system. (a) Shows the mean intensity map. (b), (c) Show second-order super-resolved pictures from the SOFI$^{(2)}$ and QSIPS$^{(2)}$ approaches, respectively. (d), (e) Demonstrate the integration of the SOFI and QSIPS methods with SIM, labeled SOFI$^{(2)}$ − SIM and QSIPS$^{(2)}$ − SIM, respectively. (f) Displays a normalized 1D plot along the dashed line in (e) for all super-resolution approaches. The simulations assume 90% optical losses (excluding the PSF effect), a blinking probability $b_\alpha = 0.1$ and $M_\alpha = 100$ excitation cycles per frame for all the emitters, RMS readout noise of 0.23, and 5×10^3 independent frames per value of θ and ϕ. (g)–(l) Refer to the same quantities of the top panels, albeit for an experimental realization performed on a cluster of colloidal QDs. The experimental setup utilized a 200 ms exposure duration, 500 μW laser power, and 5×10^2 frames per value of θ and ϕ. To increase the quality, all pictures underwent Fourier interpolation and Gaussian filtering.

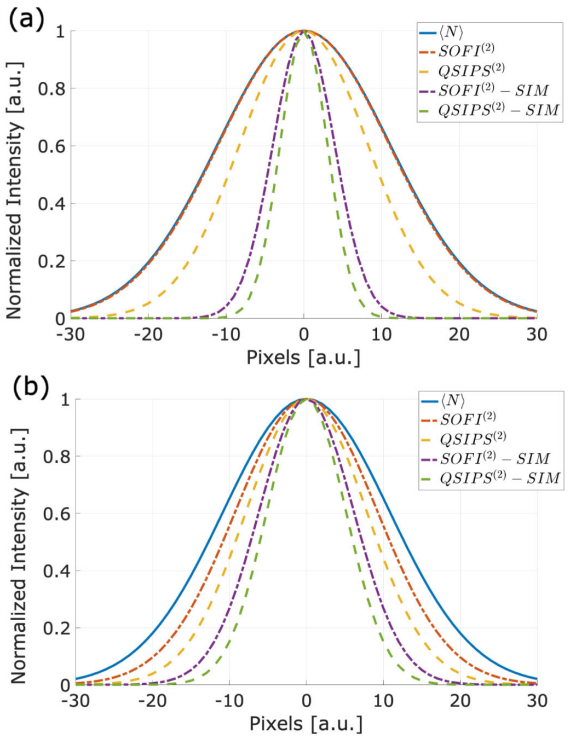

Fig. 6. 1D Gaussian fit of the effective PSF of a single emitter. (a) Depicts a simulated emitter in a noisy detection system, with blinking probability $b_\alpha = 0.1$ and $M_\alpha = 10^2$ excitation cycles per frame, and Gaussian readout noise $RMS = 0.23\mathrm{e}^-$. (b) Shows the same analysis performed experimentally on a single emitter with the same settings as per Figs. 5(g)–5(l).

theoretical values, is reported in Table 1. The super-resolution enhancement factor for SOFI$^{(2)}$ in the simulation-based scenario is compatible with 1, confirming the inadequacy of this approach in low-light scenarios, in particular when the condition in Eq. (12) is fulfilled. As a result, the super-resolution enhancement of SOFI$^{(2)}$ − SIM does not reach the theoretical value of $\sqrt{2}+2$. Nevertheless, both QSIPS$^{(2)}$ and QSIPS$^{(2)}$ − SIM simulations match their theoretically expected resolution factors. These results demonstrate that the QSIPS, including its integration with structured light, offers benefits over standard SOFI. However, the Fano factor of the measured photon distribution approaches the threshold value of 2, in which quantum fluctuation contributions start to become less important. Particularly, in the experiment, the brightness was set to achieve a compromise between producing an adequate signal-to-noise ratio for pursuing an accurate quantitative data analysis while also demonstrating QSIPS's clear advantage over SOFI. Furthermore, QSIPS$^{(2)}$ matches the theoretical super-resolution factor of $\sqrt{2}$, while the value for QSIPS$^{(2)}$ − SIM is less than the expected one of $2+\sqrt{2}$. A possible explanation for this discrepancy is that the theoretical resolution assumes $|\mathbf{p}_\theta| = k_{\mathrm{Abbe}}$. However, because the value of $|\mathbf{p}_\theta|$ is obtained from an experimental image, working at that frequency is challenging due to the optical system's low transmission at that spatial frequency. In the experiment, we select $|\mathbf{p}_\theta| < k_{\mathrm{Abbe}}$, which simplifies the SIM reconstruction but decreases the effective resolution enhancement.

5. CONCLUSION

In this paper, we introduced a general quantum approach to super-resolution imaging by photon statistics evaluation, named QSIPS, which improves by far and extends the classical techniques, such as SOFI. The QSIPS is applicable to all non-Poissonian emitters, and it is optimized at any fluorescence intensity level. Moreover, the number of images required by the fourth-order QSIPS and second-order QSIPS–SIM is comparable to that needed by typical SMLM-based techniques as reported in the literature (see [4]), demonstrating the feasibility of our method. With commercially available SPAD wide-field cameras capable of 10^5 frame/s [46], we can calculate that QSIPS–SIM maps of order 2, 3, and 4 require 0.1, 2, and 40 s, respectively, without considering the additional time needed to change the angle and phase of the structured illumination pattern.

We established the accuracy of the methods through simulations and experimental work, comparing the performance to those obtained using the standard SOFI technique. Our findings show that the QSIPS outperforms the standard SOFI method, particularly in contexts of sub-Poissonian and weak super-Poissonian photon statistics.

Furthermore, this paper examines the integration of QSIPS with structured light illumination for second-order signals, using both simulation and experiment. Additionally, in this case, the advantages with respect to the equivalent methods are particularly pronounced in low-light conditions. Although the QSIPS–SIM approach could not attain the expected theoretical resolution increase due to flaws in frequency vector evaluation, it nonetheless demonstrates novel possibilities for creating a low-power, high-resolution imaging methodology, which might be very useful in future biological applications.

Funding. European Metrology Programme for Innovation and Research (20FUN02); HORIZON EUROPE Reforming and enhancing the European Research and Innovation system (101113901); Compagnia di San Paolo; Ministero dell'Università e della Ricerca; Instituto Nazionale di Fisica Nucleare.

Acknowledgment. This work has received funding from the following projects: Project 20FUN02 POLight of the EMPIR program co-financed by the Participating States and from the European Union's Horizon 2020 research and innovation program; Qu-Test project, which has received funding from the European Union's Horizon Europe Research and Innovation Programme; Project Qutenoise of San Paolo Foundation; Project Phoenicis of "bandi a cascata" PNRR NQSTI; Project INFN QUISS.

Author contributions. I. Ruo-Berchera and I. P. Degiovanni elaborated the idea and the concept of the experiment that was executed mainly by F. Picariello, with contributions from E. Losero, S. Ditalia Tchernij, and P. Boucher. The data analysis and simulations were performed by F. Picariello. F. Picariello and I. P. Degiovanni with the help of I. Ruo-Berchera elaborated the final theoretical

Table 1. Super-Resolution Enhancement

	SOFI$^{(2)}$	QSIPS$^{(2)}$	SOFI$^{(2)}$ − SIM	QSIPS$^{(2)}$ − SIM
Simul ($F^{(d)} = 1.03 \pm 0.02$)	1.01 ± 0.02	1.40 ± 0.02	2.63 ± 0.02	3.42 ± 0.02
Exp ($F^{(d)} = 1.8 \pm 0.1$)	1.2 ± 0.1	1.4 ± 0.1	1.8 ± 0.1	2.3 ± 0.1
Th	1.4	1.4	3.4	3.4

model. M. Genovese is the group leader and supervised the project with I. Ruo-Berchera and I. P. Degiovanni. This paper was written with the contribution of all authors, while the first draft was written by F. Picariello.

Disclosures. The authors declare no conflicts of interest.

Data availability. Data underlying the results presented in this paper are not publicly available at this time but may be obtained from the authors upon reasonable request.

Supplemental document. See Supplement 1 for supporting content.

REFERENCES

1. S. Sahl, S. Hell, and S. Jakobs, "Fluorescence nanoscopy in cell biology," Nat. Rev. Mol. Cell Biol. **18**, 685–701 (2017).
2. E. Abbe, "Beiträge zur theorie des mikroskops und der mikroskopischen wahrnehmung," Arch. für Mikroskop. Anatom. **9**, 413–468 (1873).
3. S. W. Hell and J. Wichmann, "Breaking the diffraction resolution limit by stimulated emission: stimulated-emission-depletion fluorescence microscopy," Opt. Lett. **19**, 780–782 (1994).
4. M. Lelek, M. T. Gyparaki, G. Beliu, *et al.*, "Single-molecule localization microscopy," Nat. Rev. Methods Primer **1**, 39 (2021).
5. E. Betzig, G. H. Patterson, R. Sougrat, *et al.*, "Imaging intracellular fluorescent proteins at nanometer resolution," Science **313**, 1642–1645 (2006).
6. Y. Xu, R. Xu, Z. Wang, *et al.*, "Recent advances in luminescent materials for super-resolution imaging via stimulated emission depletion nanoscopy," Chem. Soc. Rev. **50**, 667–690 (2021).
7. V. Marx, "Is super-resolution microscopy right for you?" Nat. Methods **10**, 1157–1163 (2013).
8. P. P. Laissue, R. A. Alghamdi, P. Tomancak, *et al.*, "Assessing phototoxicity in live fluorescence imaging," Nat. Methods **14**, 657–661 (2017).
9. S. Wäldchen, J. Lehmann, T. Klein, *et al.*, "Light-induced cell damage in live-cell super-resolution microscopy," Sci. Rep. **5**, 15348 (2015).
10. N. P. Mauranyapin, L. Madsen, M. Taylor, *et al.*, "Evanescent single-molecule biosensing with quantum-limited precision," Nat. Photonics **11**, 477–481 (2017).
11. T. Dertinger, R. Colyer, G. Iyer, *et al.*, "Fast, background-free, 3D super-resolution optical fluctuation imaging (SOFI)," Proc. Natl. Acad. Sci. USA **106**, 22287–22292 (2009).
12. D. Cevoli, R. Vitale, W. Vandenberg, *et al.*, "Design of experiments for the optimization of SOFI super-resolution microscopy imaging," Biomed. Opt. Express **12**, 2617–2630 (2021).
13. M. Pawlowska, R. Tenne, B. Ghosh, *et al.*, "Embracing the uncertainty: the evolution of SOFI into a diverse family of fluctuation-based super-resolution microscopy methods," J. Phys. Photon. **4**, 012002 (2021).
14. A. Classen, J. von Zanthier, and G. S. Agarwal, "Analysis of super-resolution via 3D structured illumination intensity correlation microscopy," Opt. Express **26**, 27492–27503 (2018).
15. O. Solomon, M. Mutzafi, M. Segev, *et al.*, "Sparsity-based super-resolution microscopy from correlation information," Opt. Express **26**, 18238–18269 (2018).
16. M. Genovese, "Real applications of quantum imaging," J. Opt. **18**, 073002 (2016).
17. I. R. Berchera and I. P. Degiovanni, "Quantum imaging with sub-Poissonian light: challenges and perspectives in optical metrology," Metrologia **56**, 024001 (2019).
18. M. D'Angelo, M. V. Chekhova, and Y. Shih, "Two-photon diffraction and quantum lithography," Phys. Rev. Lett. **87**, 013602 (2001).
19. T. Ono, R. Okamoto, and S. Takeuchi, "An entanglement-enhanced microscope," Nat. Commun. **4**, 2426 (2013).
20. B. J. Lawrie, P. D. Lett, A. M. Marino, *et al.*, "Quantum sensing with squeezed light," ACS Photon. **6**, 1307–1318 (2019).
21. H. Defienne, W. P. Bowen, M. Chekhova, *et al.*, "Advances in quantum imaging," Nat. Photonics **18**, 1024–1036 (2024).
22. G. Brida, M. Genovese, and I. Ruo Berchera, "Experimental realization of sub-shot-noise quantum imaging," Nat. Photonics **4**, 227–230 (2010).
23. N. Samantaray, I. Ruo-Berchera, A. Meda, *et al.*, "Realization of the first sub-shot-noise wide field microscope," Light Sci. Appl. **6**, e17005 (2017).
24. G. Ortolano, C. Napoli, C. Harney, *et al.*, "Quantum-enhanced pattern recognition," Phys. Rev. Appl **20**, 024072 (2023).
25. G. Ortolano, A. Paniate, P. Boucher, *et al.*, "Quantum enhanced non-interferometric quantitative phase imaging," Light Sci. Appl. **12**, 171 (2023).
26. Y. Zhang, Z. He, X. Tong, *et al.*, "Quantum imaging of biological organisms through spatial and polarization entanglement," Sci. Adv. **10**, eadk1495 (2024).
27. R. Pooser, N. Savino, E. Batson, *et al.*, "Truncated nonlinear interferometry for quantum-enhanced atomic force microscopy," Phys. Rev. Lett. **124**, 230504 (2020).
28. C. A. Casacio, L. S. Madsen, A. Terrasson, *et al.*, "Quantum-enhanced nonlinear microscopy," Nature **594**, 201–206 (2021).
29. M. A. Taylor, J. Janousek, V. Daria, *et al.*, "Subdiffraction-limited quantum imaging within a living cell," Phys. Rev. X **4**, 011017 (2014).
30. H. Defienne, M. Reichert, J. W. Fleischer, *et al.*, "Quantum image distillation," Sci. Adv. **5**, eaax0307 (2019).
31. G. B. Lemos, V. Borish, G. D. Cole, *et al.*, "Quantum imaging with undetected photons," Nature **512**, 409–412 (2014).
32. G. Barreto Lemos, M. Lahiri, S. Ramelow, *et al.*, "Quantum imaging and metrology with undetected photons: tutorial," J. Opt. Soc. Am. B **39**, 2200–2228 (2022).
33. D. A. Kalashnikov, A. V. Paterova, S. P. Kulik, *et al.*, "Infrared spectroscopy with visible light," Nat. Photonics **10**, 98–101 (2016).
34. O. Schwartz and D. Oron, "Improved resolution in fluorescence microscopy using quantum correlations," Phys. Rev. A **85**, 033812 (2012).
35. O. Schwartz, J. M. Levitt, R. Tenne, *et al.*, "Superresolution microscopy with quantum emitters," Nano Lett. **13**, 5832–5836 (2013).
36. D. Gatto Monticone, K. Katamadze, P. Traina, *et al.*, "Beating the Abbe diffraction limit in confocal microscopy via nonclassical photon statistics," Phys. Rev. Lett. **113**, 143602 (2014).
37. M. G. Gustafsson, "Surpassing the lateral resolution limit by a factor of two using structured illumination microscopy," J. Microsc. **198**, 82–87 (2000).
38. A. Classen, J. von Zanthier, M. O. Scully, *et al.*, "Superresolution via structured illumination quantum correlation microscopy," Optica **4**, 580–587 (2017).
39. A. C. Descloux, K. S. Grußmayer, V. Navikas, *et al.*, "Experimental combination of super-resolution optical fluctuation imaging with structured illumination microscopy for large fields-of-view," ACS Photon. **8**, 2440–2449 (2021).
40. R. Tenne, U. Rossman, B. Rephael, *et al.*, "Super-resolution enhancement by quantum image scanning microscopy," Nat. Photonics **13**, 116–122 (2019).
41. A. Z. Broder, "The r-Stirling numbers," Discrete Math. **49**, 241–259 (1984).
42. A. L. Efros and D. J. Nesbitt, "Origin and control of blinking in quantum dots," Nat. Nanotechnol. **11**, 661–671 (2016).
43. A. Lal, C. Shan, and P. Xi, "Structured illumination microscopy image reconstruction algorithm," IEEE J. Sel. Top. Quantum Electron. **22**, 50–63 (2016).
44. B. Zhang, J. Zerubia, and J.-C. Olivo-Marin, "Gaussian approximations of fluorescence microscope point-spread function models," Appl. Opt. **46**, 1819–1829 (2007).
45. M. Bigas, E. Cabruja, J. Forest, *et al.*, "Review of CMOS image sensors," Microelectron. J. **37**, 433–451 (2006).
46. A. C. Ulku, C. Bruschini, I. M. Antolović, *et al.*, "A 512× 512 SPAD image sensor with integrated gating for widefield FLIM," IEEE J. Sel. Top. Quantum Electron. **25**, 1–12 (2018).